Ashley Mazurkiewicz
Department of Mechanical and
Aerospace Engineering,
Carleton University,
Ottawa, ON K1S 5B6, Canada

Sheng Xu
Department of Mechanical and
Aerospace Engineering,
Carleton University,
Ottawa, ON K1S 5B6, Canada

Hanspeter Frei
Department of Mechanical and
Aerospace Engineering,
Carleton University,
Ottawa, ON K1S 5B6, Canada

Rohan Banton
U.S. Army Research Laboratory,
Aberdeen Proving Ground,
Aberdeen, MD 21005-5066

Thuvan Piehler
U.S. Army Research Laboratory,
Aberdeen Proving Ground,
Aberdeen, MD 21005-5066;
U.S. Army Medical Research
and Development Command,
Fort Detrick, MD 21702

Oren E. Petel[1]
Department of Mechanical and
Aerospace Engineering,
Carleton University,
Ottawa, ON K1S 5B6, Canada
e-mail: oren.petel@carleton.ca

Impact-Induced Cortical Strain Concentrations at the Sulcal Base and Its Implications for Mild Traumatic Brain Injury

This study investigated impact-induced strain fields within brain tissue surrogates having different cortical gyrification. Two elastomeric surrogates, one representative of a lissencephalic brain and the other of a gyrencephalic brain, were drop impacted in unison at four different heights and in two different orientations. Each surrogate contained a radiopaque speckle pattern that was used to calculate strain fields. Two different approaches, digital image correlation (DIC) and a particle tracking method, enabled comparisons of full-field and localized strain responses. The DIC results demonstrated increased localized deviations from the mean strain field in the surrogate with a gyrified cortex. Particle tracking algorithms, defining four-node quadrilateral elements, were used to investigate the differences in the strain response of three regions: the base of a sulcus, the adjacent gyrus, and the internal capsule of the surrogates. The results demonstrated that the strains in the cortex were concentrated at the sulcal base. This mechanical mechanism of increased strain is consistent with neurodegenerative markers observed in postmortem analyses, suggesting a potential mechanism of local damage due to strain amplification at the sulcal bases in gyrencephalic brains. This strain amplification mechanism may be responsible for cumulative neurodegeneration from repeated subconcussive impacts. The observed results suggest that lissencephalic animal models, such as rodents, would not have the same modes of injury present in a gyrencephalic brain, such as that of a human. As such, a shift toward representative mild traumatic brain injury animal models having gyrencephalic cortical structures should be strongly considered.

[DOI: 10.1115/1.4050283]

1 Introduction

Mild traumatic brain injuries (mTBI) sustained through leisure activities, traffic accidents, or occupational incidents affect the health of millions of individuals worldwide annually [1,2]. Repetitive brain trauma can alter one's physical, behavioral, social, and cognitive well-being with long-term negative health outcomes [3]. Despite significant advances in the diagnosis and treatment of mTBI, detailed injury mechanisms and associated injury thresholds are still uncertain. Experimental animal model use in TBI research is widespread, in an effort to link loading conditions to injury outcomes; however, translation of these results to humans remains a challenge [4,5]. These issues of model translation are further complicated by the use of animal brain models that have limited structural similarities to a human brain, particularly with respect to cortical gyrification [6], which will necessarily result in dissimilar tissue loading conditions. In this study, we developed an experimental model, involving phantom brain surrogate slices, to investigate the influence of brain gyrification on the strain fields, specifically the strain concentrations, generated by the impact events.

The cortex of mammalian brains is composed of intimately coupled gray and white matter regions, consisting of billions of neuronal cell bodies and axons, which are the communication pathways within the brain [7]. Brain trauma has been linked to evidence of an alteration in these neural pathways of the brain. One of the suspected leading mechanisms for these changes is axonal damage through shear or axial deformation [8]. Over the long-term, repetitive brain trauma can potentially lead to neurodegeneration [9]. Postmortem analyses of brains suspected of impact-induced neurodegeneration has revealed insoluble deposits of p-tau protein positive astrocytic and neurofibrillary tangles which lead to neuronal death, primarily seen around the sulci regions of the brain [10–12].

While the accumulation of tau protein at these locations is observed well after injury has occurred [13], and the preferential concentration of these deposits at the base of the sulci suggests a geometric strain localization aspect to the injury. Strain localizations within the complex geometry of the cortical structures may be a confounding factor contributing to the injurious outcomes of the impact trauma. Geometric variations will result in a focused amplification of mean strain levels in the immediate area surrounding a geometric variation in the tissues, suggesting that the base of sulci are more susceptible to damage. Even a modest strain field applied to the complex cortex structure may lead to local strain conditions at the base of a sulcus that is twice to three

---

[1] Corresponding author.

Manuscript received July 17, 2020; final manuscript received February 8, 2021; published online March 24, 2021. Assoc. Editor: Brittany Coats.

times greater that of the mean strain field with increased shear loads. A gyrencephalic brain (e.g., human) will feature injury modalities that cannot be not present in a lissencephalic brain at similar mean strain fields.

In the study of TBI, various experimental animal models have been used to investigate pathologies related to TBI. In vitro models are able to observe injury on a molecular and cellular level by focusing on one type of tissue or cell and determining the level of injury related to specific loading conditions [14–17]. These surrogates are typically, but not exclusively, derived from rodent brains. The drawback of in vitro studies is the lack of surrounding brain structures and gyrification that can provide factors that influence the loading paths experienced by the individual cells, which may be more complex than simply hydrodynamic in nature. Brain tissue has an anisotropic composite structure that complicates extrapolating its failure behaviors based on studies of its individual components.

Ex vivo models of injury allow researchers to preserve the structures within the brain that may influence the loading scenarios. Bottlang et al. [18] used organotypic hippocampal slices from rats to induce injury. They observed that peak displacements and longitudinal elongations were increased as velocity increased; wherein injury was statistically significant at velocities over 8 m/s, corresponding to peak elongations over 25% of the sample. Sarntinoranont et al. [19] used coronal slices of rat brain and subjected these slices to high strain rates to mimic TBI scenarios. Through digital image correlation (DIC), it was determined that the rat brain tissue experienced normal strains that ranged between −0.77 and 0.56, while shear strains varied from −0.48 to 0.67 [19]. TBI research has primarily focused on this type of model, but issues arise with scaling laws and translation of the results across species [20,21], particularly when the differences between the gyrencephalic outer cortex of human brains are compared to the lissencephalic nature of the rodent brains [22].

For low-level impact events, a dominant mechanism of strain-induced damage to brain structures would be strain concentrations that results from complex human brain geometry. Furthermore, low-level rotational perturbations performed on living human participants have shown that the peak shear strains experienced in the brain are localized around geometric variations in the brain [23]. This result demonstrates the importance of using animal models with a more developed cortex, such as porcine models. Porcine brains are quite similar to human brains in both material properties and gray/white matter ratios, and have been used extensively to investigate injury thresholds [24,25]. The advantage of a porcine model of TBI is the gyrencephalic brain structure that enables investigations of the influence of naturally occuring strain concentrations on localized injury. For example, Lauret et al. [26] subjected sagittal sections of porcine brains to acceleration/deceleration trauma. The sulci and gray/white matter boundaries showed increased variations in strain and displacements as determined by DIC [26]. Raghupathi et al. [27] subjected neo-natal porcine brains to repetitive rotational loads and observed an increased accumulation of axonal damage in porcine brains, specifically localized at the sulci and gyri.

Cross-species comparisons of cortical gyrification are inherently complicated by the scaling aspects that arise. Alternative approaches, such as tissue surrogate testing and computational modeling, can provide further insights into the role of cortical gyrification on injury. Cloots et al. [28] investigated a simplified computational model of a cortex with a basic surface structure and demonstrated that strain concentrations occurred at the apex of an indentation on a surface. As head injury models increase in their complexity, a proper accounting of the distributions of strain within the brain will be required. Computational models of head injury are moving in the direction of gyrencephalic brain domains to improve model biofidelity [29].

In this study, two elastomeric phantom brain surrogates of coronal brain slices were prepared with different degrees of cortical gyrification to investigate the influence of brain gyrification on the displacement and strain fields that develop under impact loading. These surrogates had identical size and overall shape, except that one had a smoothed outer cortex and the other had a gyrified cortex, which allowed for this direct experimental comparison between a gyrencephalic and lissencephalic brain. Differences between these two surrogates under the same loading conditions can show key locations where variations of displacement and strain occur, as well as providing a bound on the expected level of strain influence from brain geometry. Observing the dynamic response of the two surrogates can reveal locations of strain concentrations and provide insights into locations within the brain that are more vulnerable to repeated low-level injury.

2 Experimental Methodology

In order to evaluate the effect of cortical gyrification on the internal strain fields of a porcine brain, a series of drop impact experiments were conducted on tissue-simulating surrogates that were representative models of coronal porcine brain tissue slices. The strain field within the surrogates was measured using an in situ high-speed X-ray (HSXR) system. HSXR was chosen over optical high-speed cameras to avoid the possibility of optical distortion from the deforming elastomers used in the containment and surrogate system.

2.1 Brain Tissue Surrogate Preparation. A set of brain tissue surrogates were prepared based on a coronal slice of a porcine brain. These surrogates were designed based on an open source MRI scan of a domestic pig brain [30]. To produce the tissue model, an image of the most visually complex coronal section of the brain (Fig. 1(*a*)) was obtained using an image visualization application, three-dimensional Slicer [31]. For comparison purposes, a photograph of a fresh porcine brain is shown in Fig. 1(*b*). An image of the tissue slice was subsequently imported into computer-assisted design software, where it was converted into two separate solid models. The first model was representative of the visually complex and gyrified cortex geometry (Fig. 1(*d*)), while a second model represented a smoothed-cortex version of the same coronal slice (Fig. 1(*c*)). The gyrified surrogate was simplified slightly from the actual brain tissue MRI, combining several gyri to form fewer and larger gyri for this study, as well as

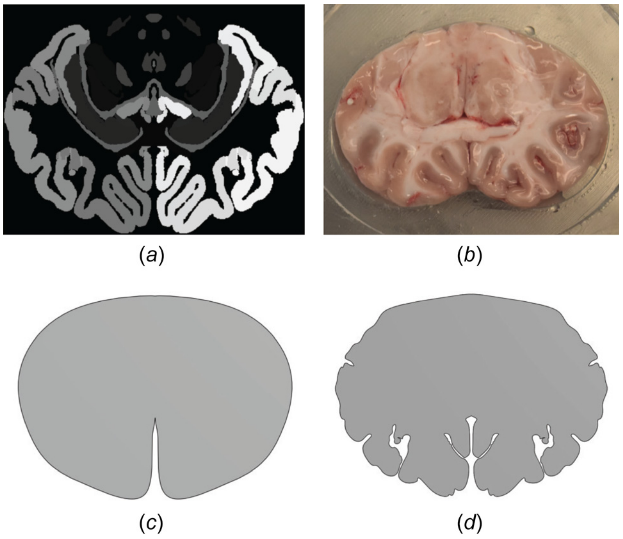

Fig. 1 (*a*) The MRI scan of a coronal porcine brain section taken from Saikali et al. [30] and visualized with three-dimensional Slicer [31]; (*b*) a photograph of a coronal section of ex vivo porcine tissue for comparison; (*c*) the smooth surrogate based on the MRI scan in (*a*), but smoothed to represent a brain with no gyrification; and (*d*) the complex surrogate followed the outline of the MRI scan in (*a*)

closing in the internal capsule regions. This simplification was necessary to allow a sufficient number of interrogation points to be integrated into the cortex to make meaningful measurements. The smooth cortex surrogate did not include any cortical gyrification details, except for the distinction between hemispheres (Fig. 1(*c*)). These two surrogate geometries were then printed using a Stratasys Dimension SST1200ES (Stratasys Inc., Rehovot, Israel) at a representative porcine brain size (56 mm × 42 mm). Inverse molds of the two samples were created using Smooth On Mold Max 30 Silicone.

In order to image the impact event using HSXR, a set of radiopaque marker sheet molds was designed to match the unique geometry of each sample. These marker sheets were designed to be embedded near the midplane of the tissue-simulant to track its deformation. In order to ensure proper dynamic coupling between the marker sheet and tissue simulant, the marker sheet was designed with a series of holes that were subsequently filled with a nonradiopaque tissue-simulant to provide contrast in HSXR images. These holes were tracked across images to track surrogate deformation during impact testing. The two radiopaque marker sheets were cast from a mixture of 50% by weight barium sulfate (Alfa Aesar) and a thermoplastic gel, Gelatin 4 (Humimic Medical). The radiopaque mixture was poured in a liquid state into the appropriate mold and cooled. In a separate mold, the brain slice surrogate was cast from a mixture of Sylgard 527 and Sylgard 184 (Dow Corning) in a 5:1 mass ratio, which has a Young's Modulus of approximately 130 kPa [32]. Polydimethylsiloxane elastomers, such as these, have been commonly used as tissue and brain simulants [33,34]. The casting of the surrogate was done in three steps: (*i*) the mold was filled one-fifth the way and allowed to partially cure at 120 °C for approximately 10 min (or until tacky to touch); (*ii*) the marker sheet was placed onto the partially cured Sylgard layer; (*iii*) the molds were then completely filled with the remaining Sylgard mixture and placed in the oven for approximately 45 min at a temperature of 120 °C to assure that the speckle sheet did not melt.

Drop testing of the tissue-simulating slices required a containment system to ensure consistent loading of the samples and provide an equally compliant boundary condition. The encasements were also prepared from the exact same 5:1 mass ratio mixture of Sylgard 527 and 184 that was used to prepare the tissue-simulating surrogates [32]. Each encasement set, which had an appearance similar to an elastomeric petri-dish, consisted of a cap and a base with a hollow cavity for sample placement. The cavity was designed to prevent the edges of the surrogate from touching its contours during an impact, so that the only boundary condition on the surrogates would be along the cut surface. The encasement was designed to hold the samples with consistent boundary conditions, allow them to be in a fluidized environment, and withstand repeated impacts. When assembled, the encasement was cuboid shaped (100 mm × 80 mm × 22 mm).

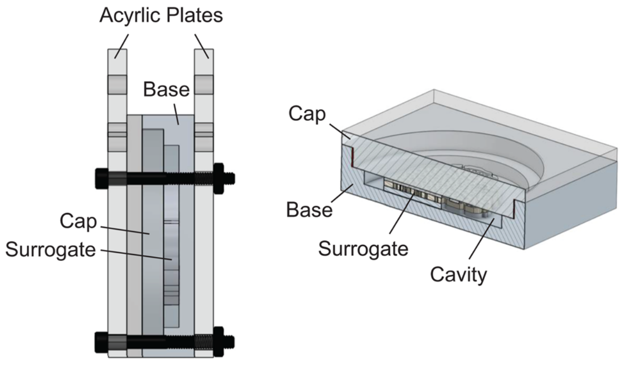

(*a*) (*b*)

Fig. 2 Schematics of (*a*) a side-on view of the encasement-surrogate assembly and (*b*) an isometric cut-away view of the encasement system

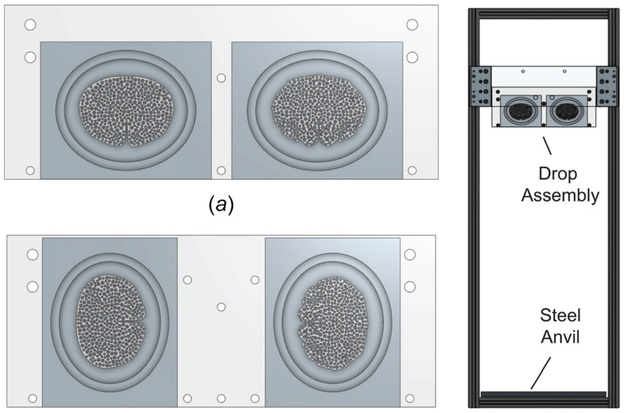

(*a*)
(*b*) (*c*)

Fig. 3 Orientations of the surrogates with smooth (left) and gyrified (right) cortical regions facing (*a*) downward and (*b*) laterally. (*c*) A schematic of the drop assembly on the drop tower and steel anvil.

Table 1 Summary of the drop heights and corresponding impact speeds

Drop height	Impact orientation	Impact speed
30 cm	Downward	2.1 m/s
50 cm	Downward	2.8 m/s
70 cm	Downward	3.4 m/s
90 cm	Downward	3.6 m/s
50 cm	Lateral	2.8 m/s

2.2 Drop Testing of Brain Tissue-Simulating Surrogates.

In preparation for the drop experiment, each brain-simulating surrogate was placed into an elastomer encasement that was subsequently sealed with silicone caulking and sandwiched between two acrylic plates. A side-on and isometric view of the encasement system is shown in Figs. 2(*a*) and 2(*b*). The lateral boundary of the surrogate was supplied by the base and cap of the encasements, which consisted of the same elastomeric materials as the surrogate. A compressive boundary condition that prevented slip of the surrogates within the elastomeric encasement was achieved by keeping the distance between the two acrylic plates constant at 34.6 ± 0.2 mm. Once the acrylic plate spacing was set, the encasements were filled with water via syringe to mimic cerebrospinal fluid. The acrylic plates, wide enough to accommodate two encasement/surrogate assemblies, were mounted to the drop assembly for a single drop event. This setup enabled a direct comparison between experiments involving both surrogates under identical drop conditions. Schematics of the tissue orientations within the drop assembly and the configuration of the drop carriage on the drop tower are shown in Fig. 3. As seen in Fig. 2(*b*), the elastomer encasement system formed a package that was flush-mounted with the base of the acrylic plates and impacted the anvil as a package. As such, the load was primarily transferred to the surrogate via the motion of the lateral confinement as well as the pressure of the fluid surrounding the surrogate.

The HSXR system captured images of the impact events with a frame rate of 7500 fps and was oriented perpendicular to the surrogate drop direction. For comparison purposes, both surrogates were dropped together in the downward orientation from four different heights (30 cm, 50 cm, 70 cm, and 90 cm) onto a rigid steel

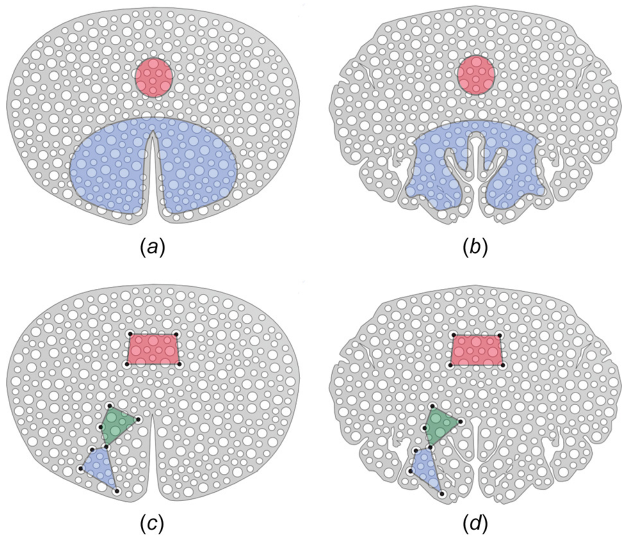

Fig. 4 Two sets of schematics indicating the regions of the surrogates analyzed in this study. Regions of the internal capsule and cortical region used in a comparison of DIC results for surrogates with (*a*) a smooth cortical region and (*b*) a gyrified cortex. Quadrilateral elements defined within the internal capsule, sulcus, and gyrus region that were used for a comparison for strain calculations from direct particle tracking techniques for surrogates with (*c*) a smooth cortical region and (*d*) a gyrified cortex.

anvil (Fig. 3(*c*)). The laterally oriented samples were only dropped from the 50 cm height. A summary of the impact speeds, calculated from the videos, for these drop tests is provided in Table 1. As both surrogates were dropped at the same time, comparisons were made between impacts at identical drop conditions. While these impacts were not meant to replicate any specific impact injury event, the strain rates involved in these tests were similar to those measured in fall or impact injury ($10^1\ \mathrm{s}^{-1}$).

2.3 Image Processing and Analysis.

MATLAB was used for all image processing needs, such as contrast adjustments and distortion corrections. A MATLAB-based open-source DIC software, Ncorr [35], was used to computationally track the motion of the radiopaque markers in the sequence of X-ray images. A domain boundary, the region of interest, was defined for each surrogate that matched closely to their specific cortical geometries. The motion tracking analysis used every other frame, and motion was tracked for a total of 32 ms following the initial impact. The resulting displacement fields tracked in the images were used to calculate the strain fields, which were then mapped onto the samples. Two regions were identified for comparison within the internal capsule and the cortical region, as shown in Figs. 4(*a*) and 4(*b*). The results returned by Ncorr provide pixelwise strain responses within the region of interest, that were used to determine the maximum and minimum principal strains (MPS and mPS, respectively) based on the equation

$$\varepsilon_{1,2} = \frac{\varepsilon_{xx} + \varepsilon_{yy}}{2} \pm \sqrt{\left(\frac{\varepsilon_{xx} - \varepsilon_{yy}}{2}\right)^2 + \left(\frac{\varepsilon_{xy}}{2}\right)^2} \tag{1}$$

where ε_1 and ε_2 represent the maximum and minimum principal strains, respectively. The dominant source of uncertainty in this analysis is due to the signal to noise ratio of the X-ray images that are subject to various sources of random shot noise. The uncertainty in the strain measurements was estimated to be approximately 0.2% strain, based on a prior study of X-ray DIC [36].

A second technique was used to map the motion of individual contrast markers in the images. This allowed us to focus on the response of specific regions of the surrogates, such as specific areas of the cortex, a technique which is being developed for use in ex vivo pig brain tissues. Mosaic Particle Tracker [37], an open-source particle tracking software add on to Fiji [38] (a distribution of IMAGEJ [39]), was used to analyze the motion of the individual markers during and following the impact event. Every frame was tracked for a total of 32 ms. The measurement uncertainty for this analysis was related to the subpixel jitter of the particle tracking algorithm, which was measured to be of the order of 0.1 mm for this work. The translation of this error to the strain analysis depends on the scale of the elements investigated. In this work, the strain error from these experiments was estimated to be as large as 0.3% strain. A series of markers were selected to define a series of four-node bilinear quadrilateral elements [40] for analysis in regions of interest. Three quadrilateral elements were defined for this analysis within the internal capsule, at the base of a sulcus, and within an adjacent gyrus. These elements were used for a comparative analysis of the strain responses within those regions for the smooth and gyrified surrogates as shown in Figs. 4(*c*) and 4(*d*). The MPS, mPS, and shear strains were calculated using this approach.

3 Results

As described above, a series of drop impacts were conducted with the tissue-simulating surrogates in a variety of orientations (see Fig. 3). The two surrogates had overt gyrencephalic differences. The first surrogate had two uniform hemispheres with smoothed outer edges, whereas the second had two hemispheres divided into two protrusions, representing cortical gyrification within the brain (see Fig. 1). The data collection approach focused on reducing variability between samples and tests to allow for direct comparisons between the strain responses of the two surrogate geometries. While the general shapes were different, the marker placement on the radiopaque sheet was nearly identical between surrogates, allowing for a direct marker to marker comparison across surrogates.

3.1 Digital Image Correlation.

The DIC analysis, using Ncorr [35], was conducted with the parameters listed in Table 2. A set of sample strain-mapped images are shown in Fig. 5 for the surrogate with the smooth cortex after a drop in the downward orientation from a height of 50 cm. A similar set of strain fields are shown in Fig. 6 for the surrogate with a gyrified cortex from the exact same drop event.

A visual comparison between surrogates with smooth (Fig. 5) and gyrified (Fig. 6) cortical geometries showed specific differences in the strain responses experienced by the surrogates for the same drop conditions, specifically in the cortical regions. The gyrified surrogate produced higher strain concentrations throughout the cortical region. For a more quantitative comparison of these differences, a statistical representation of the principal strain responses were plotted in Fig. 7 in two regions of the surrogates, the internal capsule and cortical regions. These two regions are outlined in Figs. 4(*a*) and 4(*b*), encompassing 600 and 4745 individual strain responses (pixel-based values), respectively. This comparison included both MPS and mPS responses within these

Table 2 Parameters used in the DIC analysis

Parameter name	Parameter value
Subset spacing	0
Subset radius	15
Iteration number cutoff	50
Strain radius	15

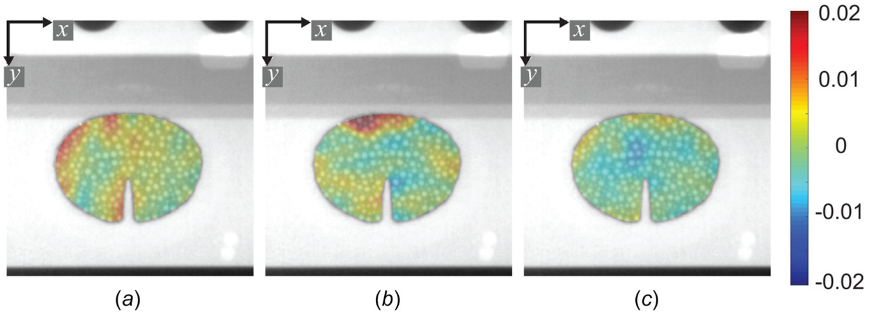

Fig. 5 DIC strain fields from the surrogate with a smooth cortex, dropped in the downward orientation from 50 cm. Each image corresponds to a specific strain distribution occurring at 3.2 ms after initial contact with the steel anvil: (*a*) ε_{xx}, (*b*) ε_{yy}, and (*c*) ε_{xy}.

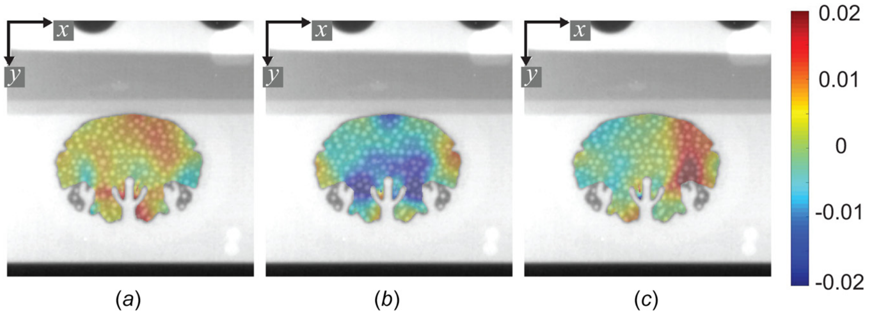

Fig. 6 DIC strain fields from the surrogate with a gyrified cortex, dropped in the downward orientation from 50 cm. Each image corresponds to a specific strain distribution occurring at 3.2 ms after initial contact with the steel anvil: (*a*) ε_{xx}, (*b*) ε_{yy}, and (*c*) ε_{xy}.

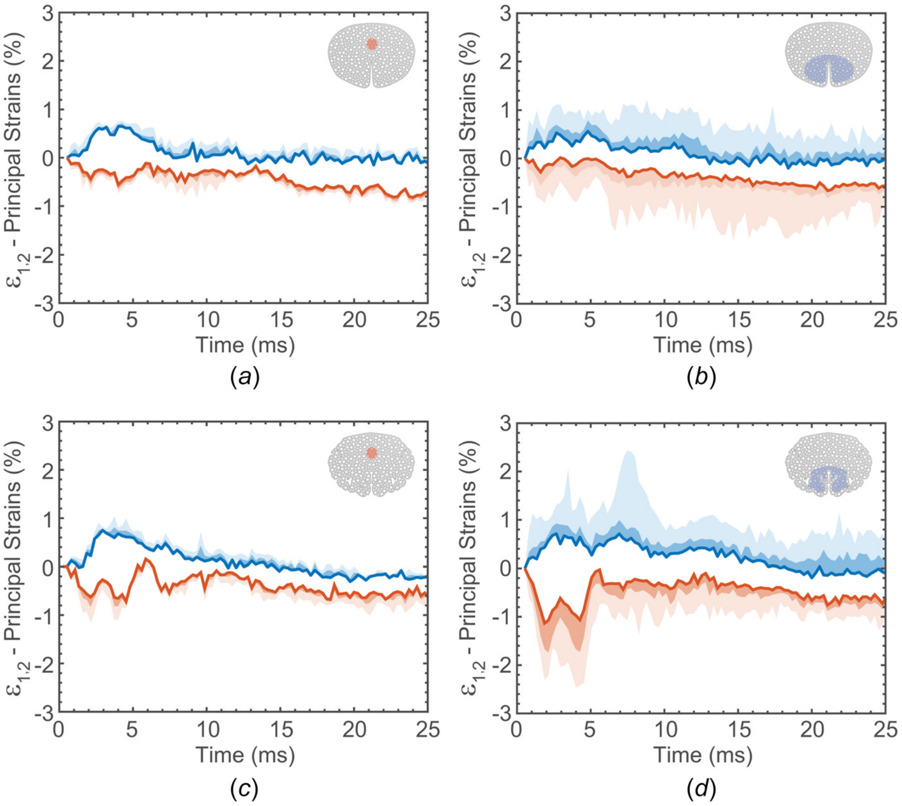

Fig. 7 The MPS and mPS strain responses for a downward-oriented drop from a 50 cm height are shown in (*a*) the internal capsule region of the surrogate with a smooth cortex, (*b*) the cortical region of the surrogate with a smooth cortex, (*c*) the internal capsule region of the surrogate with a gyrified cortex, and (*d*) the cortical region of the surrogate with a gyrified cortex. The thick lines represent the mean principal strain values, while the darker and lighter shades represent the 75th and 95th percentile principal strain values, respectively.

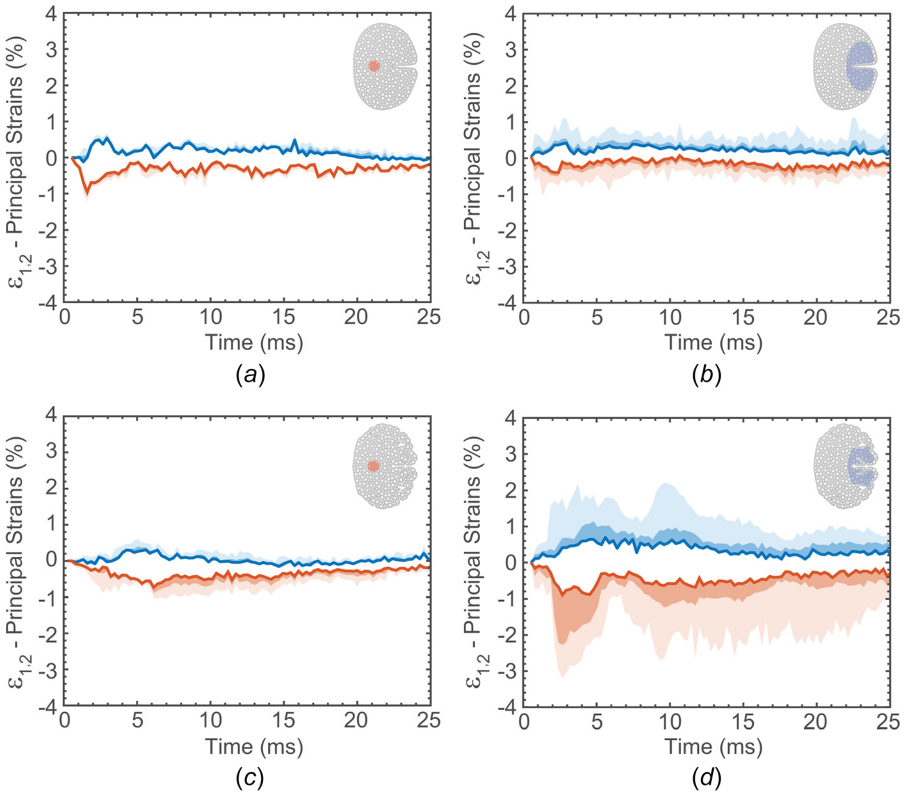

(*a*) (*b*)

(*c*) (*d*)

Fig. 8 The MPS and mPS strain responses for a laterally oriented drop from a 50 cm height are shown in (*a*) the internal capsule region of the surrogate with a smooth cortex, (*b*) the cortical region of the surrogate with a smooth cortex, (*c*) the internal capsule region of the surrogate with a gyrified cortex, (*d*) the cortical region of the surrogate with a gyrified cortex. The thick lines represent the mean principal strain values, while the darker and lighter shades represent the 75th and 95th percentile principal strain values, respectively.

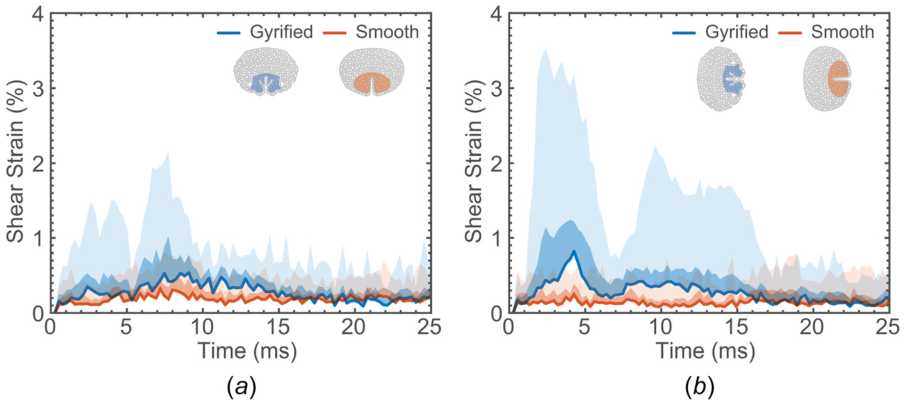

(*a*) (*b*)

Fig. 9 The shear strain responses measured in the cortical region of the surrogate with the smooth cortex and the gyrified cortex for a 50 cm drop in (*a*) a downward orientation and (*b*) a lateral orientation. The thick lines represent the mean shear strain value, while the darker and lighter shades represent the 75th and 95th percentile shear strain values, respectively.

two regions for the two surrogates. The thick lines represented the mean values within these regions, while the darker and lighter shaded regions represented the 75th and 95th percentile strains for a given region, respectively. The results in Fig. 7 illustrated that while the mean strains within the internal capsule and cortical regions did not differ substantially in their peak values, the deviations from this mean strain were greatest in the cortical regions and these deviations depended greatly on the degree of cortical gyrification. The mean strain rates measured from these impacts were of the order of $10^1\ \mathrm{s}^{-1}$.

The same comparison was made for the laterally oriented surrogate dropped from a 50 cm height (Fig. 8). In this impact orientation, the differences between the two surrogates were even more pronounced. The gyrified surrogate (Fig. 8(*d*)) recorded strain levels in the cortical region that were three times larger than those measured in the smooth surrogate (Fig. 8(*b*)). The deviations of

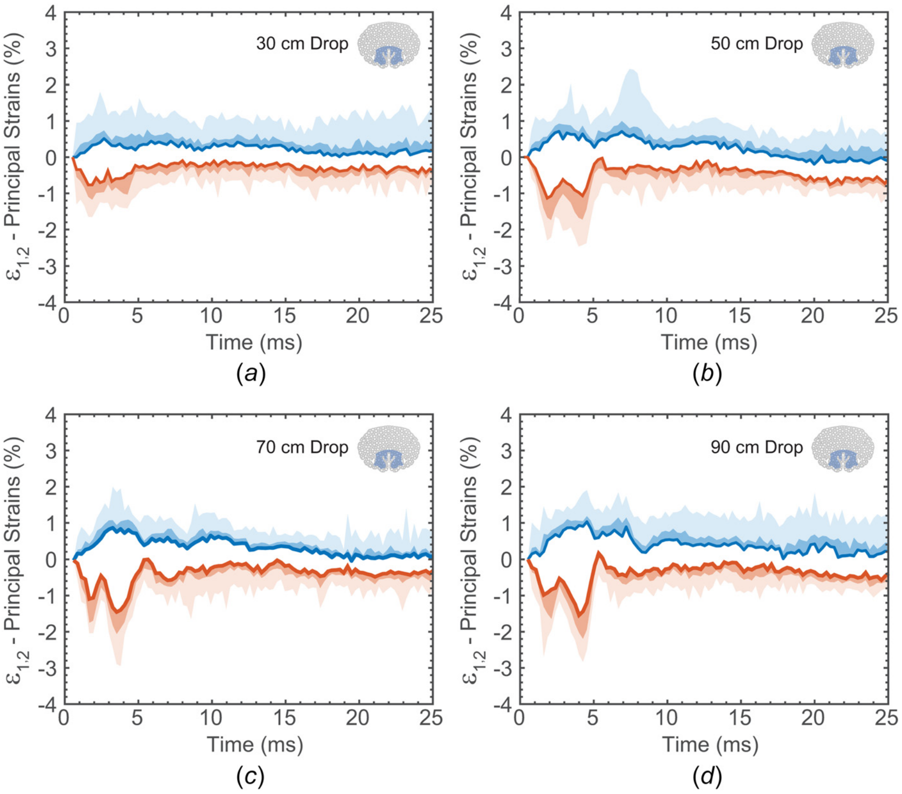

(*a*) (*b*) (*c*) (*d*)

Fig. 10 The MPS and mPS responses measured in the cortical region of the gyrified surrogate in the downward orientation for drop heights of (*a*) 30 cm, (*b*) 50 cm, (*c*) 70 cm, and (*d*) 90 cm. The thick lines represent the mean principal strain values, while the darker and lighter shades represent the 75th and 95th percentile principal strain values, respectively.

the principal strain levels within the gyrified cortex (Fig. 8(*d*)) deviated substantially from those in its internal capsule (Fig. 8(*c*)) under the laterally oriented drop impact. The trends in the principal strain values of the surrogates in the laterally oriented drop (Fig. 8) were quite similar to those seen in the downward drop orientation (Fig. 7).

The shear strain responses within the cortical regions of the two surrogates in both the downward and lateral orientations were plotted together in Fig. 9. Here, we similarly observed that the shear strain values were greater in the gyrified samples under both drop conditions, while the laterally oriented drops resulted in greater shear strain levels.

The two surrogates were also dropped from different heights to determine the response at increasing impact speeds. These impact tests resulted in differences in the principal strain levels measured within the cortex, as would be expected. Figure 10 displays the maximum and minimum principal strain values, within the gyrified surrogate, at drop heights of 30 cm, 50 cm, 70 cm, and 90 cm.

3.2 Particle Tracking Analysis. While the results in Sec. 3.1 showed a clear trend of increased strain values for increasing cortical gyrification, DIC algorithms are known to produce computational errors at the domain boundaries. These strain errors may appear as high strain concentrations along the boundaries that can be magnified by the smoothing parameters used in the DIC algorithms. These boundary uncertainty issues may have influenced the 75th and 95th percentile strain values in the cortical regions. Thus, a more robust approach to strain evaluation within the surrogates was used to investigate the strain response in different regions to look deeper into the observed strain trends. This approach involved using particle tracking algorithms to define the motion of nodes that define a series of quadrilateral elements (Figs. 4(*c*) and 4(*d*)). This enabled strain responses of specific regions to be reconciled with individual marker motions in these regions of the brain surrogates in the absence of multipixel smoothing to understand the local variability of the DIC results.

Table 3 Parameters used for the particle tracking analysis

Parameter name	Parameter value
Radius	4
Cutoff	0
Percentile	4
Link range	2
Displacement	6
Dynamics	Brownian

An open-source feature point tracking algorithm (Mosaic Particle Tracker [37]) was used to selectively track markers within the desired domain that defined a series of quadilateral elements, which were consistent across the two surrogates. The analysis was conducted with the following parameters listed in Table 3. The output from the particle tracker included x- and y-pixel trajectory coordinates according to frame number and marker tracked. In Fig. 11(*a*), a sample trajectory path obtained from Mosaic is overlaid on the initial frame at the moment of impact. Displacement histories for the markers can also be presented as x-t, y-t, or x-y plots (Figs. 11(*b*)–11(*d*)).

From these marker trajectories, and using a four-node bilinear quadilateral element formulation [40], the strain responses at the geometric center of the elements were calculated. Three elements were considered, one within the internal capsule of the surrogate, as well as elements positioned at the base of a sulcus and within a gyrus in the gyrified surrogate. The comparison of the principal strain responses for these three elements is shown separately for the two surrogates in the downward orientation for the four drop heights in Fig. 12. The same comparison was made for the shear

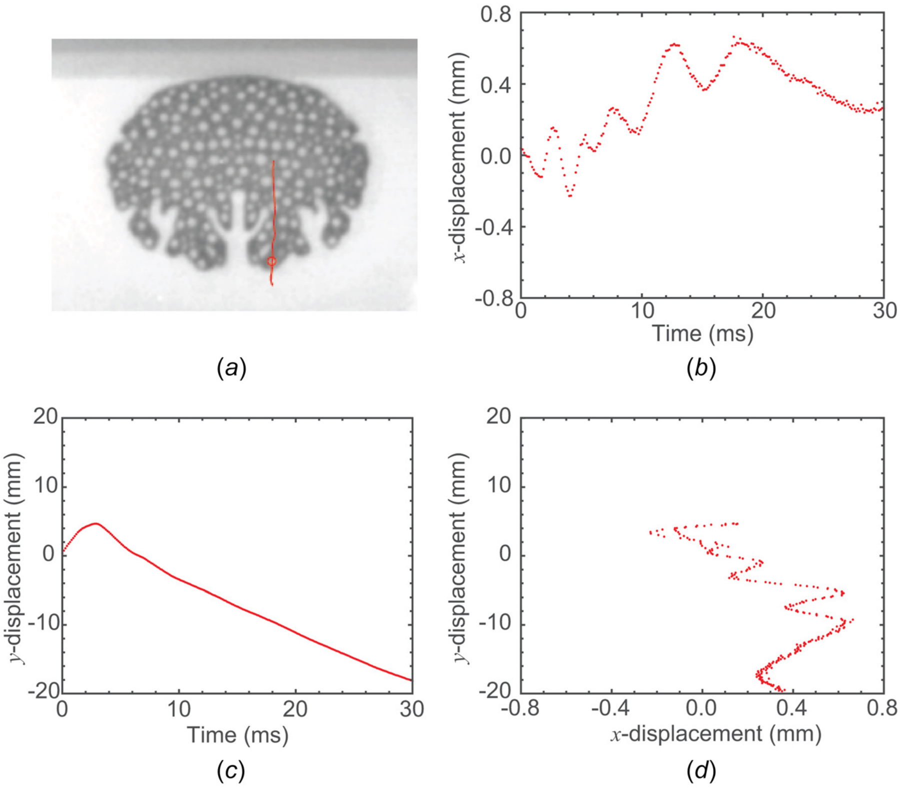

Fig. 11 Sample data from one trial of the gyrified surrogate being dropped from 50 cm in the downward orientation. (*a*) The trajectory paths of the markers, (*b*) the *x*-displacement versus time, (*c*) the *y*-displacement versus time, and (*d*) the *x*- versus *y*-displacement.

strain within these elements in Fig. 13. The principal and shear strains in the sulcus region of the gyrified brain departed substantially from the peak strain values in the adjacent gyrus and internal capsule regions of the surrogate. The differences were most apparent in comparison to the same drop conditions in the surrogate with a smooth cortex. These plots attributed the largest variations within the strain fields of the gyrified cortex (from the DIC results in Figs. 7–10) to strain concentrations localized at the base of the sulcus. This same analysis was performed with the results from the laterally oriented surrogate dropped from a height of 50 cm, with the principal and shear strain responses shown in Figs. 14 and 15, respectively.

4 Discussion

The observations from both the full-field DIC and particle tracking-based strain calculations were consistent, demonstrating similar trends in the measured strain responses and magnitudes within the tissue-simulating surrogates. The cortical regions exhibited the greatest strain variations in both surrogates; however, marked differences were seen within the gyrified and smooth cortex of the surrogates. The strain response from the midbrain to the outer cortex was dominated by the presence of gyrification, which was common in all of the DIC responses. These impacts were not meant to replicate any specific impact injury event, but resulted in strain rates that are similar to those measured in fall or impact injury, (10^1 s^{-1}). Similarly, the strain levels would be considered to be below estimated thresholds for diffuse axonal injury [41]. The low strain levels were chosen for these tests to investigate strain concentrations in a subthreshold impact injury, such as those that may lead to a cumulative neurodegeneration scenario [42].

The anatomical regions of the brain that corresponded to the large magnitudes of strain were found in cortical regions, which is seen qualitatively in the comparison of the DIC strain fields in the smooth (Fig. 5) and gyrified surrogates (Fig. 6). The results of the 50 cm drop condition with a downward-oriented cortex in Fig. 7 showed that despite the similarities in the mean strains within the internal capsule region and the cortical region, the distribution and deviations of strain within these regions are more intense in the cortex. The gyrified surrogate (Fig. 7(*d*)) displayed a broader variation in its range of strains over those measured in the smooth surrogate (Fig. 7(*b*)). The same trend was seen in the shear strain distributions within these cortical regions that were plotted in Fig. 9(*a*). The direct marker analysis that was performed for these experiments provided more information with respect to the variations within these specific regions, focusing on the strain within several quadrilateral elements. The comparisons of the principal strains for the same 50 cm drop experiments were plotted for the smooth (Fig. 12(*c*)) and gyrified (Fig. 12(*d*)) surrogate. Notice that all three elements were indistiguishable within the smooth surrogate (Fig. 12(*c*)). For the gyrified surrogate (Fig. 12(*d*)), the strain response within the internal capsule and gyrus are once again indistinguishable, however the strain within the element at the base of the sulcus is notably larger. The same trend is repeated at every drop height in Fig. 12. The results for shear strain (Fig. 13) showed the same response in the three elements investigated at all drop conditions. This response would suggest that the high strains seen in the cortical region of the gyrified sample was not generated primarily by the compression of the gyrus, but rather its motion leading to a strain concentration at the sulcus base.

These regions and the localization of strain within the cortex at the base of the sulcus, correspond precisely to areas of the brain that have shown the highest levels of accumulation of neurofibrillary entanglements in postmortem examinations [43]. These results suggest that the motion of the gyri and resulting concentrated load at the base of the sulci is a probable mechanical cause of tissue damage, even in cases where the bulk brain tissues are not subjected to excessive loads and strains. The ratio of peak

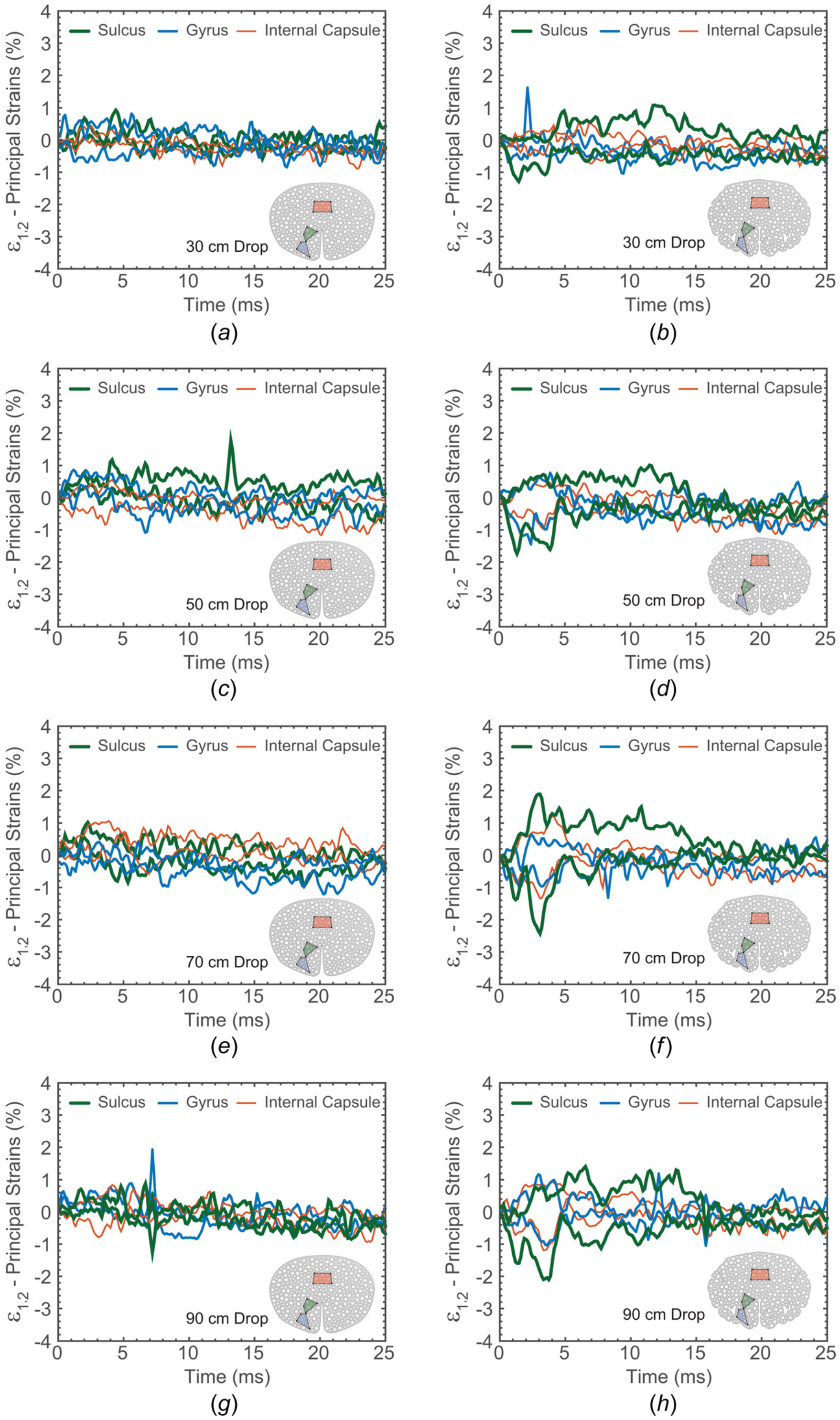

(*a*) (*b*)

(*c*) (*d*)

(*e*) (*f*)

(*g*) (*h*)

Fig. 12 A comparison of the maximum and minimum strains at the base of a sulcus, within the adjacent gyrus, and within the internal capsule for four drop conditions: (*a*) smooth cortex—30 cm drop height, (*b*) gyrified cortex—30 cm drop height, (*c*) smooth cortex—50 cm drop height, (*d*) gyrified cortex—50 cm drop height, (*e*) smooth cortex—70 cm drop height, (*f*) gyrified cortex—70 cm drop height, (*g*) smooth cortex—90 cm drop height, and (*h*) gyrified cortex—90 cm drop height

strain in the vicinity of the gyri was determined to be of the order of between 2 and 4 times the strain in the midbrain of our experimental model. As seen when comparing markers at the sulcus and gyrus on the same protrusion these strain concentrations are most notable. This level of strain variation was not observed for the deformation of the surrogate with a smooth cortex. Margulies et al. [44] used primate skulls filled with an elastomer and series of grid lines to observe strain fields under rotation, noting that the peak strains were dependent on the peak angular acceleration and skull size of the model. Given that the cortical gyrification was not included in that model, the current results suggest that those measured strains were an underestimate of the

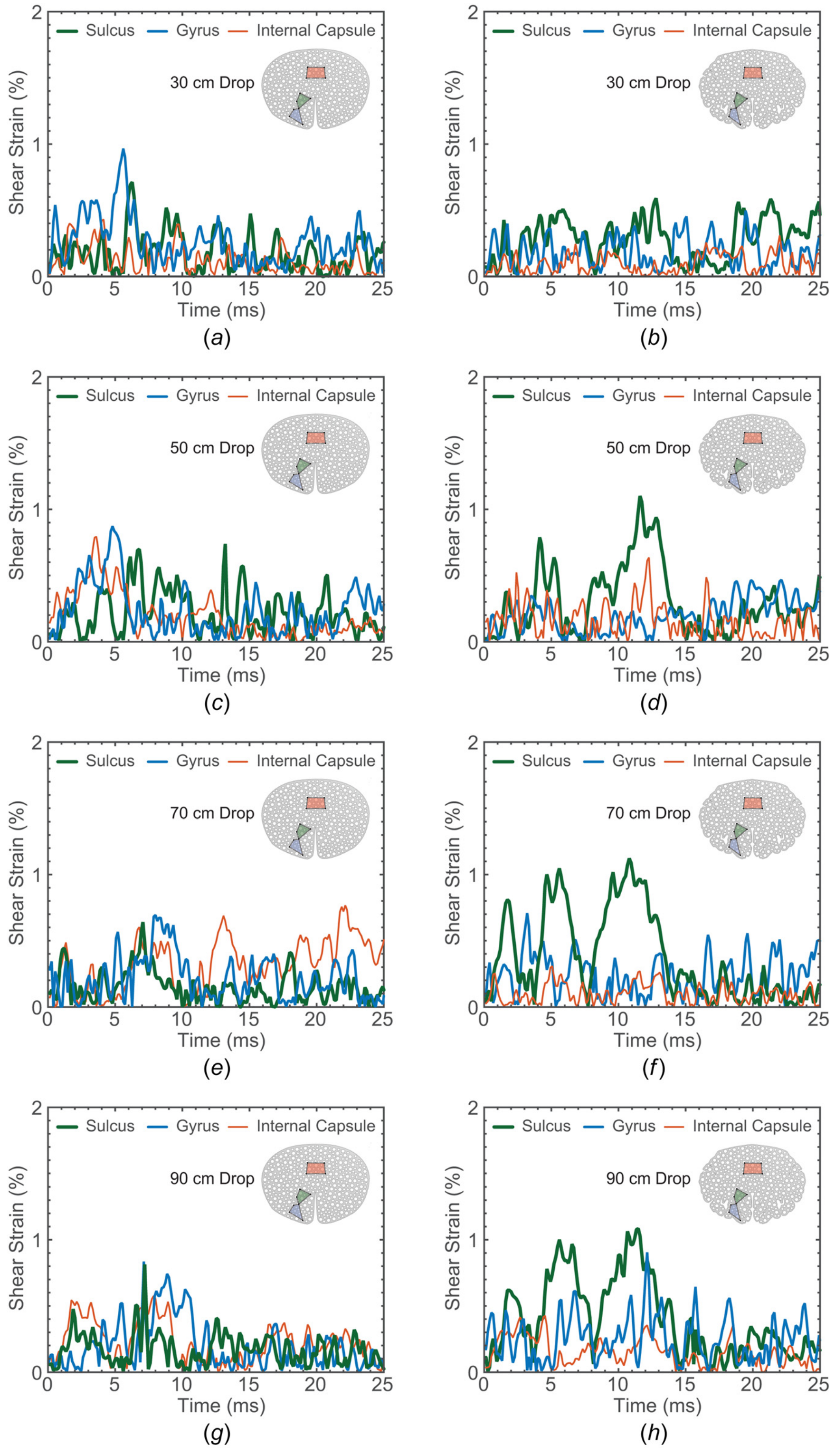

Fig. 13 A comparison of the shear strains at the base of a sulcus, within the adjacent gyrus, and within the internal capsule for four drop conditions: (*a*) smooth cortex—30 cm drop height, (*b*) gyrified cortex—30 cm drop height, (*c*) smooth cortex—50 cm drop height, (*d*) gyrified cortex—50 cm drop height, (*e*) smooth cortex—70 cm drop height, (*f*) gyrified cortex—70 cm drop height, (*g*) smooth cortex—90 cm drop height, and (*h*) gyrified cortex—90 cm drop height

true maximum strains that would have been seen at the sulcal base of a gyrified cortical structure.

Two impact orientations were investigated in this study, which provided some evidence of an influence of impact directionality on the response of a gyrified cortex. The aforementioned strain concentrations observed at the base of the sulcus, were even more pronounced in the laterally oriented impact, which induced a significant amount of motion within the brain structures. In a trend that was similar to the downward-oriented impacts, the laterally-oriented configuration produced DIC-measured strains that were

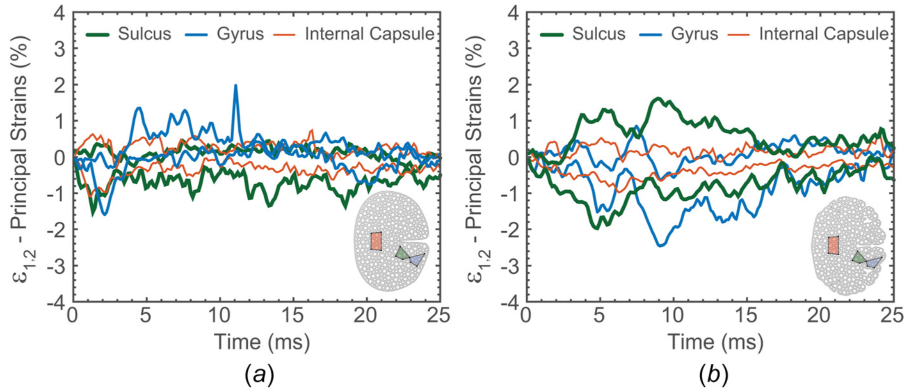

Fig. 14 A comparison of principal strains at the base of a sulcus, within the adjacent gyrus, and within the internal capsule for a laterally oriented drop from a 50 cm height are shown in (*a*) the surrogate with a smooth cortex and (*b*) the surrogate with a gyrified cortex

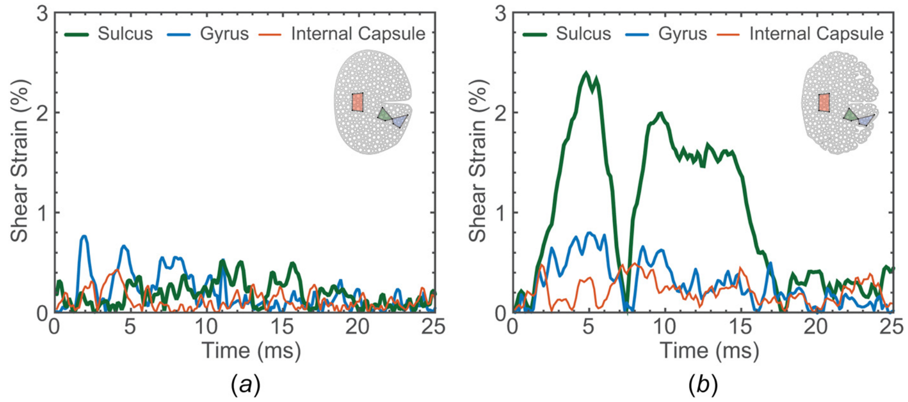

Fig. 15 A comparison of the shear strains at the base of a sulcus, within the adjacent gyrus, and within the internal capsule for a laterally oriented drop from a 50 cm height are shown in (*a*) the surrogate with a smooth cortex and (*b*) the surrogate with a gyrified cortex

also amplified in the cortical region of the gyrified surrogate (Figs. 8(*c*) and 8(*d*)). Interestingly, the laterally oriented drop of the surrogate with a smooth cortex (Figs. 8(*a*) and 8(*b*)) did not show significant variation in the DIC results. The differences in the strain fields attributed to cortical gyrification were even more pronounced in the shear strain responses of the two surrogates for a laterally oriented drop (Fig. 9(*b*)). The particle tracking and elemental strain analysis showed the same trends, whereby the principal strain level in the three regions of the surrogate were within the same range in the smooth cortex (Fig. 14(*a*)), while the sulcus and gyrus strains in the gyrified cortex exceeded the strains in the internal capsule (Fig. 14(*b*)). The difference in shear strain localization were most pronounced in the shear strain responses at the base of the sulcus in the gyrified brain (Fig. 15). The present results clearly show an influence of the impact orientation on strain fields within a gyrified cortex, indicating that some impact orientations are more detrimental than others due specifically to these strain concentrations that are influenced by the local brain gyrification. The amplification of the strains, measured at the sulcal bases, may be a mechanical mechanism that explains the cumulative injury seen from repeated subconcussive impacts.

5 Conclusions

In this study, two brain tissue surrogates representative of coronal porcine brain tissue slices, having distinct cortical geometries, were impacted and their strain responses were measured and compared. The differences in the measured strain response of these surrogates, based on both DIC and particle tracking measurements, were shown to be a result of the differences in their cortical gyrification. The sample with a gyrified cortex experienced greater strain variations, particularly in the vicinity of the base of the major sulcus. The sulcus response was contrasted to the response of the gyrus and internal capsule, showing evidence of strain and shear localizations that were concentrated at this location. In contrast, the smooth surrogate experienced minimal strain fluctuations. This mechanical mechanism of increased strain is consistent with neurodegenerative markers observed in postmortem analyses and suggests a mechanism of local damage due to strain amplification at the sulcal bases in gyrencephalic brains. This strain amplification mechanism may be responsible for cumulative neurodegeneration from repeated subconcussive impact.

The observed results suggest that lissencephalic animal models (e.g., rodent) would not have the same modes of injury present in a gyrencephalic brain (e.g., human), where peak strains that deviate from the bulk response were concentrated in specific regions of the gyrified cortex. As such, a shift toward representative mTBI animal models having gyrencephalic cortical structures should be strongly considered. This is of particular concern for rodent models of mTBI involving impact testing, as the impact response of the lissencephalic structure of a rodent brain is not consistent with humans, leading to different injury modalities. Probable injury pathways and mechanisms as well as neuron-level changes may be biased by the choice of animal model.

Acknowledgment

This research received financial support from the Department of the Army, U.S. Army Research Office under contract WP911F-

17-2-0222. Oren Petel acknowledges the financial support for the HSXR from the Canadian Foundation for Innovation and the Ontario Research Fund under project 39233. The authors thank Scott Dutrisac for useful discussions related to this work.

Funding Data

- Canada Foundation for Innovation (Grant No. 39233; Funder ID: 10.13039/501100001805).
- U.S. Army (Grant No. WP911F-17-2-0222; Funder ID: 10.13039/100006751).

References

[1] Taylor, C. A., Bell, J. M., Breiding, M. J., and Xu, L., 2017, "Traumatic Brain Injury-Related Emergency Department Visits, Hospitalizations, and Deaths—United States, 2007 and 2013," MMWR Surveillance Summaries, **66**(9), pp. 1–16.

[2] Daneshvar, D. H., Nowinski, C. J., McKee, A. C., and Cantu, R. C., 2011, "The Epidemiology of Sport Related Concussion," Clin. J. Sport Med., **30**(1), pp. 1–17.

[3] Centers for Disease Control and Prevention, 2015, "Report to Congress on Traumatic Brain Injury in the United States: Epidemiology and Rehabilitation," National Center for Injury Prevention and Control, Division of Unintentional Injury Prevention, Atlanta, GA.

[4] Panzer, M. B., Wood, G. W., and Bass, C. R., 2014, "Scaling in Neurotrauma: How Do we Apply Animal Experiments to People?," Exp. Neurol., **261**, pp. 120–126.

[5] Xiong, Y., Mahmood, A., and Chopp, M., 2013, "Animal Models of Traumatic Brain Injury," Nat. Rev. Neurosci., **14**(2), pp. 128–142.

[6] Vink, R., 2018, "Large Animal Models of Traumatic Brain Injury," J. Neurosci. Res., **96**(4), pp. 527–535.

[7] Patestas, M., and Gartner, L., 2006, *A Textbook of Neuroanatomy*, Blackwell Publishing, Malden, MA.

[8] McKee, A. C., and Robinson, M. E., 2014, "Military-Related Traumatic Brain Injury and Neurodegeneration," Alzheimer's Dementia, **10**(3 Suppl), pp. S242–S253.

[9] McKee, A. C., Cantu, R. C., Nowinski, C. J., Hedley-Whyte, T., Gavett, B. E., Budson, A. E., Veronica, E., Lee, H.-S., Kubilus, C. A., and Stern, R. A., 2009, "TDP-43 Proteinopathy and Motor Neuron Disease in Chronic Traumatic Encephalopathy," J. Neuropathol. Exp. Neurol., **68**(7), pp. 709–735.

[10] McKee, A. C., Stein, T. D., Nowinski, C. J., Stern, R. A., Daneshvar, D. H., Alvarez, V. E., Lee, H.-S., Hall, G., Wojtowicz, S. M., Baugh, C. M., Riley, D. O., Kubilus, C. A., Cormier, K. A., Jacobs, M. A., Martin, B. R., Abraham, C. R., Ikezu, T., Reichard, R. R., Wolozin, B. L., Budson, A. E., Goldstein, L. E., Kowall, N. W., and Cantu, R. C., 2013, "The Spectrum of Disease in Chronic Traumatic Encephalopathy," Brain, **136**(1), pp. 43–64.

[11] Guo, T., Noble, W., and Hanger, D. P., 2017, "Roles of Tau Protein in Health and Disease," Acta Neuropathol., **133**(5), pp. 665–704.

[12] Horstemeyer, M. F., Berthelson, P. R., Moore, J., Persons, A. K., Dobbins, A., and Prabhu, R. K., 2019, "A Mechanical Brain Damage Framework Used to Model Abnormal Brain Tau Protein Accumulations of National Football League Players," Ann. Biomed. Eng., **47**(9), pp. 1873–1888.

[13] McKee, A. C., and Daneshvar, D. H., 2015, "The Neuropathology of Traumatic Brain Injury," *Handbook of Clinical Neurology*, Vol. 127, Elsevier, Amsterdam, The Netherlands, pp. 45–66.

[14] Sawyer, T. W., Josey, T., Wang, Y., Villanueva, M., Ritzel, D., Nelson, P., and Lee, J., 2018, "Investigations of Primary Blast-Induced Traumatic Brain Injury," Shock Waves, **28**(1), pp. 85–99.

[15] Sawyer, T. W., Ritzel, D. V., Wang, Y., Josey, T., Villanueva, M., Nelson, P., Song, Y., Shei, Y., Hennes, G., Vair, C., Parks, S., Fan, C., and McLaws, L., 2018, "Primary Blast Causes Delayed Effects Without Cell Death in Shell-Encased Brain Cell Aggregates," J. Neurotrauma, **35**(1), pp. 174–186.

[16] Piehler, T., Banton, R., Zander, N., Duckworth, J., Benjamin, R., and Sparks, R., 2018, "High-Speed Imaging and Small-Scale Explosive Characterization Techniques to Understand Effects of Primary Blast-Induced Injury on Nerve Cell Structure and Function," Shock Waves, **28**(1), pp. 37–50.

[17] Thielen, P., Mehoke, T., Gleason, J., Iwaskiw, A., Paulson, J., Merkle, A., Wester, B., and Dymond, J., 2018, "Exploration of the Molecular Basis of Blast Injury in a Biofidelic Model of Traumatic Brain Injury," Shock Waves, **28**(1), pp. 115–126.

[18] Bottlang, M., Sommers, M. B., Lusardi, T. A., Miesch, J. J., Simon, R. P., and Xiong, Z.-G., 2007, "Modeling Neural Injury in Organotypic Cultures by Application of Inertia-Driven Shear Strain," J. Neurotrauma, **24**(6), pp. 1068–1077.

[19] Sarntinoranont, M., Lee, S. J., Hong, Y., King, M. A., Subhash, G., Kwon, J., and Moore, D. F., 2012, "High-Strain-Rate Brain Injury Model Using Submerged Acute Rat Brain Tissue Slices," J. Neurotrauma, **29**(2), pp. 418–429.

[20] Zhang, K., and Sejnowski, T. J., 2000, "A Universal Scaling Law Between Gray Matter and White Matter of Cerebral Cortex," Proc. Natl. Acad. Sci. U. S. A., **97**(10), pp. 5621–5626.

[21] Jean, A., Nyein, M. K., Zheng, J. Q., Moore, D. F., Joannopoulos, J. D., and Radovitzky, R., 2014, "An Animal-to-Human Scaling Law for Blast-Induced Traumatic Brain Injury Risk Assessment," Proc. Natl. Acad. Sci., **111**(43), pp. 15310–15315.

[22] Tallinen, T., Chung, J. Y., Biggins, J. S., and Mahadevan, L., 2014, "Gyrification From Constrained Cortical Expansion," Proc. Natl. Acad. Sci., **111**(35), pp. 12667–12672.

[23] Ganpule, S., Daphalapurkar, N. P., Cetingul, M. P., and Ramesh, K. T., 2018, "Effect of Bulk Modulus on Deformation of the Brain Under Rotational Accelerations," Shock Waves, **28**(1), pp. 127–139.

[24] Coats, B., and Margulies, S. S., 2006, "Material Properties of Porcine Parietal Cortex," J. Biomech., **39**(13), pp. 2521–836.

[25] Hajiaghamemar, M., Wu, T., Panzer, M. B., and Margulies, S. S., 2020, "Embedded Axonal Fiber Tracts Improve Finite Element Model Predictions of Traumatic Brain Injury," Biomech. Model. Mechanobiol., **19**(3), pp. 1109–1130.

[26] Lauret, C., Hrapko, M., van Dommelen, J. A. W., Peters, G. W. M., and Wismans, J. S. H. M., 2009, "Optical Characterization of Acceleration-Induced Strain Fields in Inhomogeneous Brain Slices," Med. Eng. Phys., **31**(3), pp. 392–399.

[27] Raghupathi, R., Mehr, M. F., Helfaer, M. A., and Margulies, S. S., 2004, "Traumatic Axonal Injury is Exacerbated Following Repetitive Closed Head Injury in the Neonatal Pig," J. Neurotrauma, **21**(3), pp. 307–316.

[28] Cloots, R. J. H., Gervaise, H. M. T., Van Dommelen, J. A. W., and Geers, M. G. D., 2008, "Biomechanics of Traumatic Brain Injury: Influences of the Morphologic Heterogeneities of the Cerebral Cortex," Ann. Biomed. Eng., **36**(7), pp. 1203–1215.

[29] Ghajari, M., Hellyer, P. J., and Sharp, D. J., 2017, "Computational Modelling of Traumatic Brain Injury Predicts the Location of Chronic Traumatic Encephalopathy Pathology," Brain, **140**(2), pp. 333–343.

[30] Saikali, S., Meurice, P., Sauleau, P., Eliat, P. A., Bellaud, P., Randuineau, G., Vérin, M., and Malbert, C. H., 2010, "A Three-Dimensional Digital Segmented and Deformable Brain Atlas of the Domestic Pig," J. Neurosci. Methods, **192**(1), pp. 102–109.

[31] Fedorov, A., Beichel, R., Kalpathy-Cramer, J., Finet, J., Fillion-Robin, J.-C., Pujol, S., Bauer, C., Jennings, D., Fennessy, F., Sonka, M., Buatti, J., Aylward, S., Miller, J., Pieper, S., and Kikinis, R., 2012, "3D Slicer as an Image Computing Platform for the Quantitative Imaging Network," Magn. Resonance Imaging, **30**(9), pp. 1323–1341.

[32] Palchesko, R. N., Zhang, L., Sun, Y., and Feinberg, A. W., 2012, "Development of Polydimethylsiloxane Substrates With Tunable Elastic Modulus to Study Cell Mechanobiology in Muscle and Nerve," PLoS One, **7**(12), p. e51499.

[33] Kalcioglu, Z. I., Mrozek, R. A., Mahmoodian, R., VanLandingham, M. R., Lenhart, J. L., and Van Vliet, K. J., 2013, "Tunable Mechanical Behavior of Synthetic Organogels as Biofidelic Tissue Simulants," J. Biomech., **46**(9), pp. 1583–1591.

[34] Ouellet, S., and Philippens, M., 2018, "The Multi-Modal Responses of a Physical Head Model Subjected to Various Blast Exposure Conditions," Shock Waves, **28**(1), pp. 19–36.

[35] Blaber, J., Adair, B., and Antoniou, A., 2015, "Ncorr: Open-Source 2D Digital Image Correlation Matlab Software," Exp. Mech., **55**(6), pp. 1105–1122.

[36] Magnan, S., 2018, "Analysis of Radiographic Contrast Markers for X-Ray Digital Image Correlation of Tissue-Simulants Under Dynamic Load," M.Sc. thesis, Carleton University, Ottawa, ON, Canada.

[37] Sbalzarini, I. F., and Koumoutsakos, P., 2005, "Feature Point Tracking and Trajectory Analysis for Video Imaging in Cell Biology," J. Struct. Biol., **151**(2), pp. 182–195.

[38] Schindelin, J., Arganda-Carreras, I., Frise, E., Kaynig, V., Longair, M., Pietzsch, T., Preibisch, S., Rueden, C., Saalfeld, S., Schmid, B., Tinevez, J.-Y., White, D. J., Hartenstein, V., Eliceiri, K., Tomancak, P., and Cardona, A., 2012, "Fiji: An Open-Source Platform for Biological-Image Analysis," Nat. Methods, **9**(7), pp. 676–682.

[39] Schneider, C. A., Rasband, W. S., and Eliceiri, K. W., 2012, "NIH Image to ImageJ: 25 Years of Image Analysis," Nat. Methods, **9**(7), pp. 671–675.

[40] Cook, R. D., and Malkus, D. S., 2007, *Concepts and Applications of Finite Element Analysis*, John Wiley & Sons, Hoboken, NJ.

[41] Margulies, S. S., and Thibault, L. E., 1992, "A Proposed Tolerance Criterion for Diffuse Axonal Injury in Man," J. Biomech., **25**(8), pp. 917–923.

[42] Baugh, C., Stamm, J., Riley, D., Gavett, B., Shenton, M., Lin, A., Nowinski, C., Cantu, R., McKee, A., and Stern, R., 2012, "Chronic Traumatic Encephalopathy: Neurodegeneration Following Repetitive Concussive and Subconcussive Brain Trauma," Brain Imaging Behav., **6**(2), pp. 244–254.

[43] Mckee, A. C., Stein, T. D., Kiernan, P. T., and Alvarez, V. E., 2015, "The Neuropathology of Chronic Traumatic Encephalopathy," Brain Pathol, **25**(3), pp. 350–364.

[44] Margulies, S. S., Thibault, L. E., and Gennarelli, T. A., 1990, "Physical Model Simulations of Brain Injury in the Primate," J. Biomech., **23**(8), pp. 823–836.